Distinguishing malignant from benign microscopic skin lesions using desorption electrospray ionization mass spectrometry imaging

Katherine Margulis[a], Albert S. Chiou[b], Sumaira Z. Aasi[b], Robert J. Tibshirani[c,d], Jean Y. Tang[b], and Richard N. Zare[a,1]

[a]Department of Chemistry, Stanford University, Stanford, CA 94305; [b]Department of Dermatology, Stanford University School of Medicine, Stanford, CA 94305; [c]Department of Statistics, Stanford University, Stanford, CA 94305; and [d]Department of Biomedical Data Sciences, Stanford University, Stanford, CA 94305

Contributed by Richard N. Zare, May 8, 2018 (sent for review March 2, 2018; reviewed by R. Graham Cooks and David C. C. Muddiman)

Detection of microscopic skin lesions presents a considerable challenge in diagnosing early-stage malignancies as well as in residual tumor interrogation after surgical intervention. In this study, we established the capability of desorption electrospray ionization mass spectrometry imaging (DESI-MSI) to distinguish between micrometer-sized tumor aggregates of basal cell carcinoma (BCC), a common skin cancer, and normal human skin. We analyzed 86 human specimens collected during Mohs micrographic surgery for BCC to cross-examine spatial distributions of numerous lipids and metabolites in BCC aggregates versus adjacent skin. Statistical analysis using the least absolute shrinkage and selection operation (Lasso) was employed to categorize each 200-μm-diameter picture element (pixel) of investigated skin tissue map as BCC or normal. Lasso identified 24 molecular ion signals, which are significant for pixel classification. These ion signals included lipids observed at *m/z* 200–1,200 and Krebs cycle metabolites observed at *m/z* < 200. Based on these features, Lasso yielded an overall 94.1% diagnostic accuracy pixel by pixel of the skin map compared with histopathological evaluation. We suggest that DESI-MSI/Lasso analysis can be employed as a complementary technique for delineation of microscopic skin tumors.

basal cell carcinoma | Mohs surgery | mass spectrometry imaging | desorption electrospray ionization | microscopic tumors

One of the main goals in cancer diagnostics is the detection of microscopic tumors (<1–2 mm in diameter) in early stages, when the tumor is still confined to the site of its origin and is easy to eradicate with a localized treatment (1). Basal cell carcinoma (BCC) is a common skin cancer that, depending on the growth pattern, can be dispersed in numerous and sometimes noncontiguous micrometer-sized aggregates within the affected skin. In this study, we used human BCC specimens collected from routine Mohs surgeries to assess the capability of an ambient mass spectrometry imaging technique, desorption electrospray ionization mass spectrometry imaging (DESI-MSI), to detect the presence of microscopic tumor.

BCC is the most common form of skin cancer, with an estimated incidence of 4 million new cases diagnosed annually in the United States (2). While rarely lethal, BCC can be highly disfiguring if not diagnosed and treated promptly, because it can be locally destructive. It usually occurs on sun-exposed areas of the body, such as the face and neck. Surgical excision of BCC can also lead to functional and cosmetic deformity if a significant amount of normal skin is removed, especially when tumors involve vital structures, for example, eyelids, nose, lips, or ears. A tissue-sparing treatment modality that significantly reduces surgical morbidity with skin cancer extirpation is Mohs micrographic surgery (3). In Mohs surgery, the surgeon removes a small disk of tissue using a beveled surgical margin to obtain thin tissue sections, which are subsequently histologically stained for 360° intraoperative tumor margin assessment (Fig. 1*A*). This meticulous process is repeated until there is no residual tumor identified microscopically (Fig. 1*B*). The technique is extremely effective for BCC treatment, but the histopathologic processing is time-consuming and highly dependent on the skills and experience of the evaluating Mohs surgeon. Several normal structures and processes within the skin tissue create visual artifacts that can hamper a correct identification of tumor loci in stained sections, for example, hair follicles, inflammation, and nerve proximity (4). In these situations, an objective adjunctive technique can significantly aid in delineation of microscopic tumors without reliance on visual histopathologic evaluation.

DESI-MSI is a nondestructive imaging method that can map spatial distributions of molecules within a tissue section to discriminate between regions of varying pathology. Briefly, a beam of charged solvent droplets is directed onto the tissue surface to desorb and ionize molecules, while the splash of these droplets carries the resultant ions into a mass spectrometer for analysis (Fig. 1*C*). A 2D imaging stage moves the tissue at a controlled speed to record the mass spectra from different spatial coordinates, while the signal is subsequently converted into 2D images of molecular ion distributions (Fig. 1*C*). Recent studies by our group and others have demonstrated DESI-MSI's capability to discriminate between tumor and normal tissue for various malignancies, including brain, gastric, breast, thyroid, prostate, ovarian, kidney, and pancreatic cancers (5–14). These studies typically relied on collecting series of DESI-MS images of continuously

Significance

Timely detection of microscopic tumors is of utmost importance in cancer diagnostics. We show that desorption electrospray ionization mass spectrometry imaging (DESI-MSI) can successfully locate microscopic aggregates of a common skin cancer, basal cell carcinoma (BCC), and distinguish them from adjacent normal skin. DESI-MSI unveils an altered chemical profile in BCC region, including lipids and metabolites, and does not rely on visual identification of histopathologic features. We processed specimens from 86 Mohs micrographic surgeries, with nearly 60% of tumors sized less than 1 mm in diameter. By applying the statistical method of least absolute shrinkage and selection operator (Lasso) on collected DESI-MSI data, we were able to achieve up to 94.1% diagnostic accuracy compared with pathological evaluation of BCC.

Author contributions: J.Y.T. and R.N.Z. designed research; K.M., A.S.C., S.Z.A., and R.J.T. performed research; S.Z.A. performed histopathological evaluation of specimens; K.M., A.S.C., S.Z.A., R.J.T., J.Y.T., and R.N.Z. analyzed data; R.J.T. designed and guided statistical analysis; and K.M., A.S.C., and R.N.Z. wrote the paper.

Reviewers: R.G.C., Purdue University; and D.C.C.M., North Carolina State University.

The authors declare no conflict of interest.

Data deposition: The raw data reported in this paper have been deposited in Figshare (https://figshare.com/articles/training_txt/6332012).

[1]To whom correspondence should be addressed. Email: zare@stanford.edu.

This article contains supporting information online at www.pnas.org/lookup/suppl/doi:10.1073/pnas.1803733115/-/DCSupplemental.

Published online June 4, 2018.

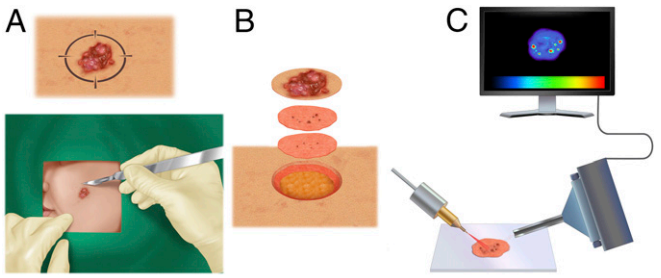

Fig. 1. General workflow of this study. (*A*) During Mohs surgery, a surgeon removes a lesion suspected as basal cell carcinoma (BCC). A 2D map of the lesion is created. (*B*) Using tissue-sparing technique, the visible tumor and a conservative margin of normal skin are removed and subsequently stained for histopathological evaluation. The process continues until the stained sections are clear of microscopic tumor aggregates. (*C*) Excised skin sections are imaged by desorption electrospray ionization mass spectrometry (DESI-MS) imaging, which can accurately delineate microscopic tumor aggregates without histological staining and evaluation.

normal or malignant specimens followed by building a statistical classifier that can discern between two types of tissue based on molecular signature obtained from the mass spectra. Note that after the classifier is built, biopsy processing does not necessarily rely on imaging and many times can be achieved with a simple DESI-MS analysis provided that the cancerous area is sufficiently large.

However, imaging mode can be imperative for tumor detection in tissues of mixed pathology. Although a typical analyte desorbing spot size in DESI-MSI is around 200 μm, DESI-MSI in certain conditions, for example, small *x*–*y* stage step size, diminished spray capillary diameter, narrow *m*/*z* scan range, and short scan time, was reported to resolve features as small as 35 μm (15). In this study, we applied DESI-MSI to delineate multiple aggregates of BCC present within normal skin in human specimens collected during routine Mohs surgeries (Fig. 1). Nearly 60% of the detected lesions were smaller than 1 mm in diameter; ∼35% were sized less than 200 μm at least in one dimension. This study shows that DESI-MSI can serve as an auxiliary diagnostic tool in Mohs micrographic surgery for skin cancers and has the ability to detect miniscule individual tumor aggregates characteristic of very early-stage malignancies.

Results

Specimen Collection and Imaging Specifications. Specimen collection occurred between August 2016 and October 2016 at the Stanford University Medical Center Mohs Surgery Clinic. This study was approved by the IRB at Stanford. Deidentified intraoperative specimens from 86 Mohs micrographic surgeries for BCC of different body sites were prospectively collected and analyzed during our study. Specimens were processed in the typical manner for Mohs surgery with no special processing or pretreatment required. After thin sections were obtained from each surgical specimen for routine Mohs histopathologic analysis, additional research sections were formed from deeper into the surgical blocks for DESI-MSI. To facilitate the practical translation of the developed diagnostic tool into a surgery setting, we employed a relatively low-cost mass spectrometer, linear trap quadrupole, LTQ XL, for imaging and analysis of the specimens. Using this mass spectrometer allowed us to achieve rapid imaging, on the order of 5–15 min per skin specimen, at a mass resolving power of ∼1,000. This rapid analysis identified a metabolic pattern that could be used to discern tumor aggregates from normal skin at high imaging speed. Five-micrometer-thick skin sections obtained from Mohs surgeries were imaged in negative-ion mode by DESI-MSI. These sections contained numerous minute aggregates of BCC sparingly dispersed within normal skin. Nearly 60% of them were smaller than 1 mm in diameter; ∼35% were sized less than 200 μm at least in one dimension (Fig. 2). These aggregates were of various histologic types of BCC, including nodular (48%), superficial (17%), and aggressive (20%), which included both infiltrative and micronodular types. A significant portion of specimens contained multiple types (15%). Some nests contained mostly connective tissue (stroma) interspersed with tumor cells. These factors resulted in high metabolic heterogeneity within the tumors. Our goal was to detect all tumor-involved areas and distinguish them from normal skin. We made no distinction between normal skin and various benign heterogeneous processes contained within it, such as inflammation, hair follicles, nerve proximity, connective tissue, vasculature, or structures of the pilosebaceous unit, and as such designated all skin free of BCC as "normal" as it would be ideally diagnosed in a Mohs surgery setting.

Multiple parameters, such as nebulizing gas flow rate, DESI-MSI spray geometry, ion injection time, and more were experimentally optimized to achieve a maximal spatial precision of imaging without compromising tissue-analyte extraction and signal intensity (*Materials and Methods*).

Molecular Imaging and Analysis. For the construction of 2D imaging maps, we first acquired the spectra in negative-ion mode in the mass to charge ratio (*m*/*z*) range of 150–1,200. This range allowed the detection of free fatty acids (FAs) (*m*/*z* 200–400), FA dimeric clusters (*m*/*z* 500–600), and complex glycerophospholipids (*m*/*z* 700–1,000). The specimens were histologically stained after imaging using hematoxylin and eosin (H&E) procedure for unfixed tissue (16).

Histopathologic assessment of various tissue regions was then performed and compared with the constructed 2D images and the mass spectra average from each region. The spectra demonstrated characteristic differences in molecular ion distribution patterns in BCC tumor aggregates versus normal skin (*SI Appendix*, Fig. S1). Some of the molecular ion signals were subsequently identified using tandem MS, high mass accuracy, and isotopic distribution (*SI Appendix*, Table S1). It should be noted that tandem-MS experiments were necessary to determine the exact length of acyl groups in glycerophospholipids, whereas the position and stereochemistry of the double bonds in FAs and glycerophospholipids could not be accurately assigned even following tandem-MS experiments.

In particular, BCC nests were distinctively rich in arachidonic acid, FA (20:4) (*m*/*z* 303.3), and glycerophosphoglycerol 34:1, PG (18:1/16:0) (*m*/*z* 747.6), and they demonstrated high relative and total abundances of oleic acid, FA (18:1) (*m*/*z* 281.3); glycerophosphoserine 36:1, PS (18:1/18:0) (*m*/*z* 788.5); palmitic acid, FA (16:0) (*m*/*z* 255.3); and glycerophosphoinositol 38:4, PI (18:0/20:4)

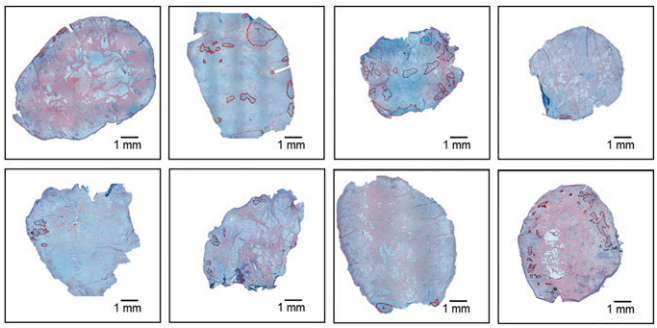

Fig. 2. Histologically stained skin sections containing miniscule basal cell carcinoma (BCC) aggregates. BCC regions are marked in red.

(*m/z* 885.6) (*SI Appendix*, Fig. S2 *A–F*). Among other molecular ions abundant in BCC regions, we could identify FA dimers at *m/z* 537.4 (oleic acid + palmitic acid), *m/z* 563.5 (oleic acid + oleic acid), and *m/z* 585.5 (oleic acid + arachidonic acid), as well as phospholipids, glycerophosphoglycerol 36:2, PG (18:1/18:1) at *m/z* 773.6 (*SI Appendix*, Fig. S2*G*); glycerophosphoserine 38:4, PS (20:4/18:0) at *m/z* 810.6 (*SI Appendix*, Fig. S2*H*); glycerophosphoinositol 34:1, PI (16:1/18:0) at *m/z* 835.6; and glycerophosphoinositol 36:2, PI (18:2/18:0) at *m/z* 861.6 (*SI Appendix*, Fig. S3 *A* and *B*, respectively).

In the adjacent normal skin, a very prominent peak was detected at *m/z* 465.4 and was unambiguously identified by high-accuracy MS and sulfur isotopic distribution as cholesterol sulfate. Cholesterol sulfate demonstrated markedly higher relative and absolute abundances in normal skin regions than in BCC lesions. However, its signal intensity distribution in the normal skin showed both significant interspecimen and intraspecimen variation, which prevented it from acting as a reliable biomarker of cutaneous pathology. Cholesterol sulfate is an important metabolite produced by sun-exposed skin that has been shown to have a variety of physiological functions (17, 18) and was also linked to skin carcinogenesis inhibition (19). However, its distribution is highly nonhomogeneous throughout the skin (20, 21), which can account for its uneven signal detected with the DESI-MSI.

Compared with BCC aggregates, normal skin regions exhibited lower relative and absolute abundances of arachidonic acid, FA (20:4) (*m/z* 303.3), and glycerophosphoglycerol 34:1, PG (18:1/16:0) (*m/z* 747.6), and showed a presence of chloride adducts of glycerophosphocholines (PCs), including glycerophosphocholine PC 34:1, PC (18:0/16:1) at *m/z* 794.4, and glycerophosphocholine 34:2, PC (18:1/16:1) at *m/z* 792.4 (*SI Appendix*, Fig. S3 *C* and *D*, respectively). A greater ratio of saturated stearic acid FA (18:0) (*m/z* 283.3) (*SI Appendix*, Fig. S3*E*) to monounsaturated oleic acid FA (18:1) (*m/z* 281.3) ion signals was also observed in many regions of normal skin. FA dimers had particularly strong ion signals at *m/z* 537.4 (oleic acid + palmitic acid) and at *m/z* 563.5 (oleic acid + oleic acid), but not at *m/z* 585.5 (oleic acid + arachidonic acid) in normal skin. Other molecular ions identified in normal skin regions included palmitic (FA 16:0) and palmitoleic (FA 16:1) acids at *m/z* 255.3 and 253.2 (*SI Appendix*, Fig. S3*F*), respectively; glycerophosphoinositols 38:4, PI (18:0/20:4), 36:2, PI (18:2/18:0), and 34:1, PI (16:1/18:0) at *m/z* 885.6, 861.6, and 835.6, respectively; and glycerophosphoserine 36:1, PS (18:1/18:0) at *m/z* 788.5 (*SI Appendix*, Fig. S1). Fig. 3 shows selected 2D DESI-MSI maps of molecular ion distribution for specimens #15-1441, #15-1372, and #16-042 with normalization to a total ion current (*Lower* panels) to account for any variations in imaging conditions between different experiments. Visual examination of the chemical maps constructed by DESI-MSI allowed us to delineate BCC aggregates in some cases. However, a reliable classification of each pixel as normal or cancer could only be achieved by applying a multivariate statistical approach.

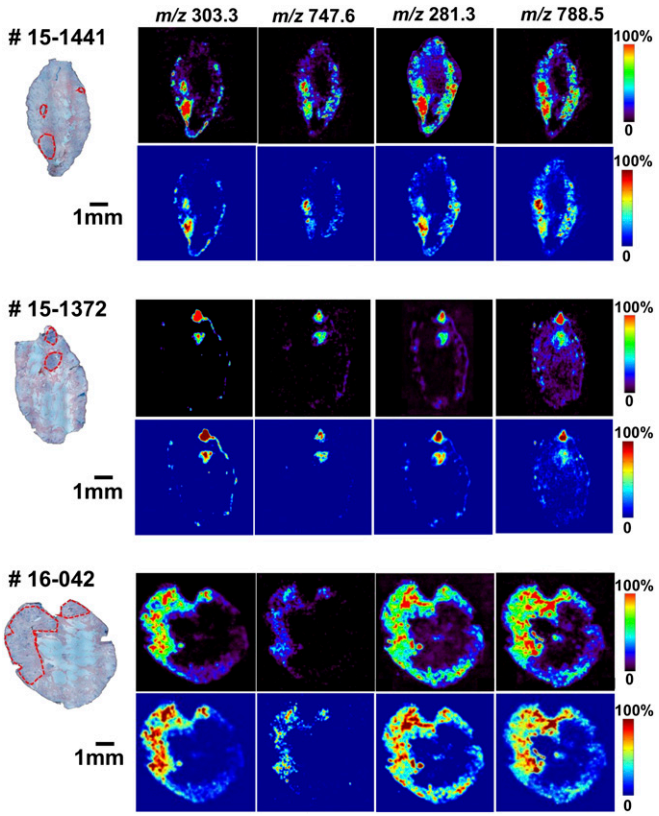

Fig. 3. Selected 2D desorption electrospray ionization mass spectrometry (DESI-MS) images of molecular ion distribution for specimens #15-1441, #15-1372, and #16-042. Molecular ion distribution (*Upper* panel of each sample) is shown with normalization to a total ion current (*Lower* panel of each sample) to account for experimental variation between different measurements.

Statistical Analysis. We used the Lasso method (22) to select statistically important ion signal peaks in the mass spectra and build a classifier that estimates the probability that each individual pixel in the DESI-MS image is BCC aggregate versus normal skin. Lasso has an exceptional ability to minimize the amount of statistically significant data, which was particularly important in this case where the spectrum of each pixel produced a large number of ion signal features. To build our Lasso classifier, a set of 17,053 pixels imaged in the range of *m/z* 50–1,200 (see below) was employed and 17-fold cross-validation was applied. Because of the dispersed nature of individual tumor islands within normal skin in the vast majority of obtained clinical samples, no group of 100% tumor specimens could be identified, and therefore the Lasso classifier was generated by delineating regions of interest diagnosed as BCC aggregates versus adjacent normal skin in randomly chosen specimens. Lasso was able to effectively shrink the amount of diagnostically significant MS data (Fig. 4) by selecting a total of 24 ion signal peaks (Table 1) that could reliably predict the histopathological diagnosis of each 200-μm-diameter pixel of investigated skin tissue map. These selected mass-spectral features are quantitative weighting factors that are predictive of BCC. Peaks abundant within a cancerous area were given a positive weight, whereas peaks with low abundance or absent in BCC received a negative weight. It is noteworthy that some of the selected peaks originate from a pair of monoisotopic and ^{13}C1 isotopic forms of the same molecular ion, which might increase a relative weight of the ion in distinguishing between normal and diseased states. In cases when the imaging is performed with high mass resolution, the ratio of the peaks may predict the molecular composition of the ion (23).

An independent test set composed of 40,001 pixels imaged in the range of *m/z* 150–1,200 served as one of the two test sets in our Lasso analysis and yielded the overall accuracy of 88.3% of correct diagnosis compared with histopathology per each 200-μm-diameter pixel (Table 2).

To further improve the diagnostic accuracy, we expanded the imaging range of DESI-MS to *m/z* 50–1,200. This enabled the detection of deprotonated Krebs cycle intermediates (Fig. 5), which mediate cellular energy metabolism and supply building blocks for intracellular lipid formation. Including these species in the Lasso analysis was recently proven to increase the accuracy of Lasso predictions (6). We used a set of 7,963 pixels imaged in the range of *m/z* 50–1,200 as the second independent test set. This test set yielded an overall accuracy of 94.1% for the correct diagnosis compared with histopathology per each 200-μm-diameter pixel (Table 2). This reduced sensitivity (77.2%) might have

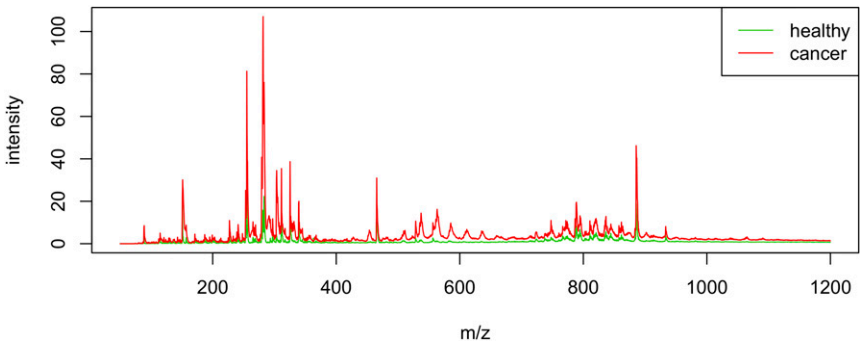

Fig. 4. The least absolute shrinkage and selection operation (Lasso) method yields a model with sets of mass-spectral features for distinguishing between basal cell carcinoma (BCC) and normal skin. The average mass spectra calculated from raw peak abundances in all pixels of the training dataset are shown in red for BCC and green for normal.

originated from the highly dispersed nature of submicron aggregates of BCC, and from the difficulty of categorizing the pixels at the BCC margin against histopathological assignment owing to their mixed pathology. Lasso identified one molecular ion signal, at *m/z* 115.0, in the expanded *m/z* range that significantly contributes to diagnostic prediction, being relatively more prevalent in the normal skin versus BCC nests.

The species detected at *m/z* 115.0 was identified by the tandem MS as singly charged fumarate (Fig. 5 and *SI Appendix*, Fig. S3*G*), a Krebs cycle intermediate naturally produced in sun-exposed skin (24).

Because fumarate is one of the key intermediates in the Krebs cycle, its levels may be disrupted by aberrant metabolism of tumors that drive toward cataplerotic production of lipids and metabolites required for cell proliferation (Fig. 5). Previously, fumarate has been shown to inhibit chemical carcinogenesis in mouse skin (25).

In this study, the Lasso was trained to differentiate BCC aggregates from normal skin, a clinically relevant aspect of Mohs surgery. It is also important to note that our specimens included various histologic types of BCC, with some specimens containing a high content of stroma. These factors led to a high metabolic heterogeneity of the tumors, which further challenged this analysis. However, high-accuracy prediction for each individual 200-μm-diameter pixel of skin map was possible using only 24 ion signal features.

Discussion

DESI-MS analysis of tissues is an increasingly employed diagnostic and prognostic tool that can rapidly map and interrogate numerous molecules and metabolites in fresh tissues without molecular labeling or compromising tissue homeostasis. Already some workers have been able to examine fresh tissue samples taken during surgery in a time of less than an hour (7) or in just a few minutes (26). DESI-MSI combined with statistical analyses has emerged as a powerful technique for evaluating intraoperative surgical margins in several cancers owing to its reasonably good resolution. In this work, we established the diagnostic capability of DESI-MS in miniscule tumors by demonstrating that it can accurately differentiate between micrometer-sized lesions of the most common skin cancer, BCC, and highly heterogeneous adjacent skin structures, such as connective tissue, vasculature, and structures of the pilosebaceous unit. Using 86 human skin specimens obtained from Mohs surgery of BCC, we showed that DESI-MSI coupled with Lasso effectively discriminates aggregates of BCC less than 200 μm in size at least in one dimension from normal skin structures at an accuracy of 94% of correct diagnosis compared with histopathology per each 200-μm-diameter pixel of skin map. These minuscule dimensions of delineated tumor islands suggest that DESI-MSI scan system can resolve structures smaller than the typical solvent spot size, and that it can be employed to detect very early-stage malignancy of various organs, where the tumors emerge as individual microscopic cell aggregates. This higher resolution is the result of overlapping desorption spots in a continuous spraying mode of operation. In addition, because DESI-MSI fundamentally relies upon the deranged metabolic activity of malignant tumors to differentiate them from normal tissue structures, the high accuracy achieved in a biologically indolent BCC suggests that more aggressive tumors may be even easier to recognize by DESI-MSI.

By interrogating tumor metabolic reprogramming in BCC by DESI-MSI, we identified a marked increase in relative and absolute abundances of FAs, especially arachidonic acid FA (20:4), and certain complex glycerophospholipids, such as glycerophosphoglycerol 34:1 and glycerophosphoserine 36:1. FA synthesis is the initial step in de novo lipid biosynthesis required for cancer cell proliferation and survival (27). FAs participate in a variety of metabolic pathways promoting and maintaining cellular growth (28). In particular, FA (20:4), or arachidonic acid, is a precursor of prostaglandins that were shown to be elevated in BCC compared with normal skin, and are predictive of tumor aggressiveness (29, 30). FAs are then incorporated into complex glycerophospholipids, which further promote biomass growth by providing building blocks and suitable physical properties to dividing cell membranes, acting as signaling mediators and regulating energy metabolism in cells (31). However, not all glycerophospholipids and their precursors are elevated in BCC, and the tumors present rather differential regulation of metabolites. Thus, glycerophosphocholine PC 34:1 and

Table 1. Lasso-identified important mass-spectral features, which can predict the pathology of each 200-μm-diameter pixel with high accuracy

m/z	Lasso weight	*m/z*	Lasso weight
115.0	−0.143	311.7	−0.005
150.9	−0.027	325.3	−0.009
151.3	−0.001	325.8	−0.026
253.3	+0.002	465.5	−0.005
255.5	+0.004	466.4	−0.004
279.3	+0.015	556.9	+0.002
281.3	+0.008	747.7	+0.042
282.0	+0.002	786.6	+0.001
283.5	+0.004	788.4	+0.018
303.3	+0.139	794.5	−0.040
304.1	+0.016	885.6	−0.007
311.3	−0.007	886.6	−0.003

List of 24 mass-spectral features required for prediction of pathology. Note that the analysis was performed on integrated low-resolution MS data, and therefore the *m/z* of some selected features deviate slightly from the actual masses of the peaks.

Table 2. Prediction of pathology for each 200-μm-diameter image pixel by Lasso

Set (*m/z*)	Diagnosis (for each 200-μm-diameter pixel)	Normal	BCC	Correct, %
Test set (*m/z* 150–1,200)	Normal	28,624	2,051	93.3
	BCC	2,618	6,708	71.9
	Overall agreement:			88.3
Test set (*m/z* 50–1,200)	Normal	6,435	155	97.6
	BCC	313	1,060	77.2
	Overall agreement:			94.1

Two test sets are shown.

glycerophosphoinositol 38:4 show lower abundances in tumor region. In addition, the Krebs cycle intermediate fumarate demonstrates markedly depleted levels in BCC aggregates probably owing to the increased rate of cataplerosis in tumor (32). We have previously documented the depletion of other Krebs cycle intermediates in prostate cancer (6). Hence, employing Lasso or a comparable statistical method is imperative for interrogating this differential metabolic profile of BCC. Lasso was able to discern BCC aggregates from adjacent normal skin based on only 24 mass-spectral features detected by inexpensive benchtop mass spectrometer. This opens an avenue for a rapid, intraoperative specimen analysis during Mohs surgeries that could be complementary to histopathological stained-section evaluation and could help establish fast and unambiguous diagnosis by eliminating interference of visual morphological artifacts.

Materials and Methods

Specimen Collection and Preparation. Skin specimens were prospectively collected during Mohs surgeries from August 2016 to October 2016 at the Department of Dermatology, Stanford University Medical School. This study was approved by the Stanford IRB (Protocol #24,307). The treating physician reviewed the patient information sheet with the patient in a private room, and verbal informed consent was obtained using standard consenting technique after all of the patient's questions were addressed. Patients were informed that they could withdraw from the trial at any time and their care could fully continue at Stanford without prejudice. A copy of the tissue donation information sheet was given to the patients. The specimens were processed similarly to skin sections sent to histopathological evaluation. Briefly, Mohs excisions were sectioned using a Leica CM1850 cryostat (Leica Biosystems). Five-micrometer sections of each tissue were mounted on a glass slide and sent for both pathological evaluation within the Department of Dermatology and DESI-MS analysis in the Department of Chemistry. When not analyzed immediately, these fresh specimens were stored at −80 °C and briefly dried in vacuum desiccator before DESI-MS analysis.

DESI-MS Analysis. A 2D DESI-MSI source (Prosolia) was coupled to an LTQ XLTM mass spectrometer (Thermo Scientific) for skin imaging. DESI-MSI was performed in the negative-ion mode at *m/z* ranges of 150–1,200 and 50–1,200. To desorb and ionize metabolites from skin, we used a histologically compatible solvent system, dimethylformamide:acetonitrile 1:1 (vol/vol) (HPLC-grade solvents from Sigma-Aldrich), at a flow rate of 0.7 μL/min. The nebulizing gas pressure was set to 190 psi, and the spray voltage to −5 mV. The spray tip-to-surface distance was 2 mm, spray incident angle was 56°, and the spray-to-inlet distance was 6.5 mm. The step size in the moving stage was set to 0.2 mm, capillary voltage to −65 V, tube lens voltage to −120 V, and four microscans and 80-ms maximum ion injection time were applied with a scanning speed in *x* direction of 285–294 μm/s with the automatic gain control of the mass spectrometer switched off. These parameters were empirically found to yield the optimal MS signal from skin tissues without compromising spatial resolution of the imaging. All experiments were carried out under identical experimental conditions to allow comparison between measurements. The software ImageCreator (version 3.0) was used to convert the Xcalibur 2.2 mass spectra files (Thermo Fisher Scientific) into a format compatible with BioMap (freeware, version 3.8.0.4, www.ms-imaging.org) to construct spatially accurate 2D ion images. Rainbow color palette was used in the BioMap for signal intensity visualization.

After DESI-MSI, the same skin section was subjected to H&E staining for unfixed tissue (16) and histopathologic evaluation by our Mohs surgeon (S.Z.A.), who reviewed and annotated normal and cancerous regions. These annotations were transferred into DESI-MS images. Another software, MSIReader (version 0.09) (33), was employed to normalize the images by the total ion current and to extract regions of interest for statistical analysis. To use the MSIReader, an additional freeware tool, MSConvert (tool of ProteoWizard software, version 2.1x) (34), was employed to convert the Xcalibur 2.2 mass spectra files (.raw files) into .mzML format files; then imzMLConverter (version 1.3.0) (35) was used to combine .mzML files into .imzML format file, readable by the MSIReader. Jet color palette and the fifth-order linear interpolation were used in the MSIReader for signal intensity visualization. We exported MS signal for statistical analysis as regions of BCC and normal skin without discriminating between highly heterogeneous morphological and pathological structures within normal skin, such as inflammation, necrosis, hair follicles, nerve proximity, connective tissue, vasculature, the structures of the pilosebaceous unit, and more.

For exact lipid and metabolite identification, tandem-MS and high-mass resolution analyses were performed using the LTQ-Orbitrap XL (Thermo Scientific). For lipid identification in a normal skin, a tumor-free (by histopathology) skin section was used (specimen #16-1767), whereas for lipid identification in cancer, a skin section with multiple BCC aggregates overall occupying ∼70% of the skin section area (specimen #16-1799) was used. The tissue sections were carefully removed from glass slides, and the lipids were extracted in 500 μL of methanol:water 70:30 solution. The undissolved tissue was separated from the extract by centrifugation at 4,000 × *g* for 5 min. Supernatant was collected and introduced into mass spectrometer for tandem-MS and high-mass resolution analyses via electrospray at the solvent flow rate of 5 μL/min. Nebulizing gas pressure was set to 120 psi, spray voltage was −5 mV, capillary voltage was −65 V, tube lens voltage was −120 V, ion injection time was 100 ms, and one microscan was performed, with a mass resolution of 60,000 at *m/z* 400. For the MS/MS studies, a normalized collision energy of 20–40% was applied, the isolation window width was set to 1.0 *m/z*, an activation *Q* value was 0.2–0.25, ion injection time was 1,000 ms, and one microscan was performed. The lipid compositions were assigned based on high-mass resolution analysis, isotope distribution, and tandem-MS fragmentation pattern (*SI Appendix*, Table S1). In the case when several detectable fragmentation patterns were generated by isomeric parent ions, the most intense fragmentation peaks were used to assign lipid identity listed in *SI Appendix*, Table S1. The LipidMaps (www.lipidmaps.org/),

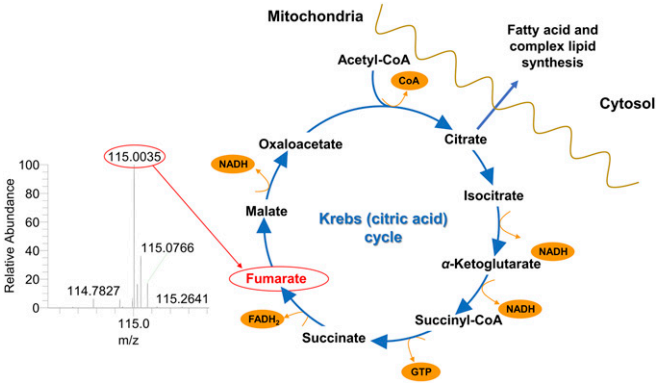

Fig. 5. Fumarate is a Krebs cycle intermediate important for Lasso analysis. It was unambiguously identified by high-resolution MS.

MassBank (www.massbank.jp), and Metlin (https://metlin.scripps.edu/) databases were employed to assist with lipid identification.

Statistical Analysis. The 2D mass spectra files obtained by DESI-MSI were converted to delimited text files (.csv format) and exported for statistical analysis according to regions of interest of varying pathology using the MSIReader (see above).

We randomly divided the specimens into training set imaged at *m/z* 50–1,200 and two sets of test specimens, one set imaged at *m/z* 150–1,200, and the second one imaged at *m/z* 50–1,200. Regions of interest were delineated within the specimens to categorize each 200-μm-diameter pixel of investigated skin map as BCC or normal skin. Lasso method (multiclass-logistic regression with L1 penalty) was applied within the training set using the glmnet 2.0-2 package in the CRAN R language library (36). Seventeen-fold cross-validation was employed, leaving out one specimen at a time, to choose the Lasso tuning parameter and to evaluate its predictive accuracy within the training set.

Lasso yields a "sparse" model containing the most informative features for the prediction task (37). In this application, the Lasso method yielded a model with parsimonious sets of mass-spectral features for discriminating between BCC and normal skin. No discrimination was made between highly heterogeneous morphological and pathological structures within normal skin, such as inflammation, necrosis, hair follicles, nerve proximity, connective tissue, vasculature, and the structures of the pilosebaceous unit, and all noncancerous skin was annotated as "normal." Also, no discrimination was made between various types of BCC as well as between stroma-rich and stroma-poor tumors. A mathematical weight for each statistically informative mass-spectral feature was calculated by Lasso depending on its importance in classifying the skin as BCC. Molecular ion signals, whose increased relative intensity was important for characterizing tumor regions, were given a positive weight, whereas molecular ion signals that had decreased intensity or were absent in BCC received a negative weight.

ACKNOWLEDGMENTS. We thank Jamaica Jensen, lead Mohs technician, and Samantha Rodriguez, Mohs technician, for their assistance in preparing specimens for this study. K.M. is grateful to the Stanford Center of Molecular Analysis and Design for supporting her fellowship. This work was supported by Air Force Office of Scientific Research Grant FA9550-16-1-0113.

1. Cao C, et al. (2014) Targeted in vivo imaging of microscopic tumors with ferritin-based nanoprobes across biological barriers. *Adv Mater* 26:2566–2571.
2. Shug AL, Paulson DJ (1984) Fatty acid and carnitine-linked abnormalities during ischemia and cardiomyopathy. *Myocardial Ischemia and Lipid Metabolism*, eds Ferrari R, Katz AM, Shug A, Visioli O (Springer, Boston), pp 203–224.
3. Tokede O, et al. (2017) Effectiveness of Mohs micrographic surgery for nonmelanoma skin cancer: A systematic review protocol. *JBI Database Syst Rev Implement Reports* 15:666–675.
4. França K, Alqubaisy Y, Hassanein A, Nouri K, Lotti T (November 10, 2016) Histopathologic pitfalls of Mohs micrographic surgery and a review of tumor histology. *Wien Med Wochenschr*, 10.1007/s10354-016-0528-0.
5. Takáts Z, Wiseman JM, Gologan B, Cooks RG (2004) Mass spectrometry sampling under ambient conditions with desorption electrospray ionization. *Science* 306: 471–473.
6. Banerjee S, et al. (2017) Diagnosis of prostate cancer by desorption electrospray ionization mass spectrometric imaging of small metabolites and lipids. *Proc Natl Acad Sci USA* 114:3334–3339.
7. Eberlin LS, et al. (2014) Molecular assessment of surgical-resection margins of gastric cancer by mass-spectrometric imaging. *Proc Natl Acad Sci USA* 111:2436–2441.
8. Calligaris D, et al. (2014) Application of desorption electrospray ionization mass spectrometry imaging in breast cancer margin analysis. *Proc Natl Acad Sci USA* 111: 15184–15189.
9. Eberlin LS, et al. (2016) Pancreatic cancer surgical resection margins: Molecular assessment by mass spectrometry imaging. *PLoS Med* 13:e1002108.
10. Jarmusch AK, et al. (2016) Lipid and metabolite profiles of human brain tumors by desorption electrospray ionization-MS. *Proc Natl Acad Sci USA* 113:1486–1491.
11. Zhang J, et al. (2016) Cardiolipins are biomarkers of mitochondria-rich thyroid oncocytic tumors. *Cancer Res* 76:6588–6597.
12. Shroff EH, et al. (2015) MYC oncogene overexpression drives renal cell carcinoma in a mouse model through glutamine metabolism. *Proc Natl Acad Sci USA* 112:6539–6544.
13. Amstalden van Hove ER, Smith DF, Heeren RM (2010) A concise review of mass spectrometry imaging. *J Chromatogr A* 1217:3946–3954.
14. Tata A, et al. (2016) Rapid detection of necrosis in breast cancer with desorption electrospray ionization mass spectrometry. *Sci Rep* 6:35374.
15. Campbell DI, Ferreira CR, Eberlin LS, Cooks RG (2012) Improved spatial resolution in the imaging of biological tissue using desorption electrospray ionization. *Anal Bioanal Chem* 404:389–398.
16. Calligaris D, et al. (2013) Mass spectrometry imaging as a tool for surgical decision-making. *J Mass Spectrom* 48:1178–1187.
17. Seneff S, Davidson RM, Lauritzen A, Samsel A, Wainwright G (2015) A novel hypothesis for atherosclerosis as a cholesterol sulfate deficiency syndrome. *Theor Biol Med Model* 12:9.
18. Strott CA, Higashi Y (2003) Cholesterol sulfate in human physiology: What's it all about? *J Lipid Res* 44:1268–1278.
19. Chida K, Murakami A, Tagawa T, Ikuta T, Kuroki T (1995) Cholesterol sulfate, a second messenger for the eta isoform of protein kinase C, inhibits promotional phase in mouse skin carcinogenesis. *Cancer Res* 55:4865–4869.
20. Epstein EH, Williams ML, Elias PM (1984) The epidermal cholesterol sulfate cycle. *J Am Acad Dermatol* 10:866–868.
21. Elias PM, et al. (1984) Stratum corneum lipids in disorders of cornification. Steroid sulfatase and cholesterol sulfate in normal desquamation and the pathogenesis of recessive X-linked ichthyosis. *J Clin Invest* 74:1414–1421.
22. Tibshirani R (1997) The lasso method for variable selection in the Cox model. *Stat Med* 16:385–395.
23. Khodjaniyazova S, et al. (2018) Characterization of the spectral accuracy of an orbitrap mass analyzer using isotope ratio mass spectrometry. *Anal Chem* 90:1897–1906.
24. Council of Europe's Committee of Experts on Cosmetic Products (2008) *Active Ingredients Used in Cosmetics: Safety Survey* (Council of Europe, Strasbourg, France).
25. Sporn MB, Liby KT (2012) NRF2 and cancer: The good, the bad and the importance of context. *Nat Rev Cancer* 12:564–571.
26. Pirro V, et al. (2017) Intraoperative assessment of tumor margins during glioma resection by desorption electrospray ionization-mass spectrometry. *Proc Natl Acad Sci USA* 114:6700–6705.
27. Baenke F, Peck B, Miess H, Schulze A (2013) Hooked on fat: The role of lipid synthesis in cancer metabolism and tumour development. *Dis Model Mech* 6:1353–1363.
28. Roongta UV, et al. (2011) Cancer cell dependence on unsaturated fatty acids implicates stearoyl-CoA desaturase as a target for cancer therapy. *Mol Cancer Res* 9: 1551–1561.
29. Rustin MH, Bull HA, Dowd PM (1987) Arachidonic acid metabolites in cutaneous carcinomas. *Arch Dermatol* 123:159.
30. Vanderveen EE, Grekin RC, Swanson NA, Kragballe K (1986) Arachidonic acid metabolites in cutaneous carcinomas. Evidence suggesting that elevated levels of prostaglandins in basal cell carcinomas are associated with an aggressive growth pattern. *Arch Dermatol* 122:407–412.
31. Liu Y, Wang W, Shui G, Huang X (2014) CDP-diacylglycerol synthetase coordinates cell growth and fat storage through phosphatidylinositol metabolism and the insulin pathway. *PLoS Genet* 10:e1004172.
32. DeBerardinis RJ (2008) Is cancer a disease of abnormal cellular metabolism? New angles on an old idea. *Genet Med* 10:767–777.
33. Robichaud G, Garrard KP, Barry JA, Muddiman DC (2013) MSiReader: An open-source interface to view and analyze high resolving power MS imaging files on Matlab platform. *J Am Soc Mass Spectrom* 24:718–721.
34. Kessner D, Chambers M, Burke R, Agus D, Mallick P (2008) ProteoWizard: Open source software for rapid proteomics tools development. *Bioinformatics* 24:2534–2536.
35. Race AM, Styles IB, Bunch J (2012) Inclusive sharing of mass spectrometry imaging data requires a converter for all. *J Proteomics* 75:5111–5112.
36. Friedman J, Hastie T, Simon N, Tibshirani R (2013) glmnet: Lasso and elastic-net regularized generalized linear models. Version glmnet 2.0-2. Available at https://cran.r-project.org/web/packages/glmnet/index.html. Accessed May 20, 2017.
37. James G, Witten D, Hastie T, Tibshirani R (2013) *An Introduction to Statistical Learning: With Applications in R* (Springer, New York).